



# Effect of process parameters on bead geometry, tensile and microstructural properties of double-sided butt submerged arc welding of SS 304 austenitic stainless steel

P. V. S. S. Sridhar<sup>1</sup> · Pankaj Biswas<sup>1</sup> · Pinakeswar Mahanta<sup>1</sup>

Received: 19 June 2019 / Accepted: 15 September 2020 / Published online: 29 September 2020  
© The Brazilian Society of Mechanical Sciences and Engineering 2020

## Abstract

The purpose of this investigation is to study the effect of welding variables on bead geometry, fusion zone profile and tensile properties of double-sided submerged arc welding on SS 304 austenitic stainless steel. The individual effect of welding parameters, i.e., welding current, voltage and traverse speed, on bead geometry and tensile properties was investigated. Both microstructural and mechanical characterizations of the weldment were carried out in the present study. It was observed that the operating parameters have significant effect on bead geometry and tensile properties. The double-sided welding effectively enhanced the weld seam ductility. The percentage of elongation is improved by 19.48% to 50.2% for double-sided samples as compared to base material. A comparative study between single and double-sided butt welding was also carried out. For single-sided sample the percentage of elongation is lower than the base material. The percentage reduction in angular distortion of 55.17% is observed with double-sided weld sample as compared to single-sided weld sample.

**Keywords** Operating parameters · Angular distortion · Tensile strength · Bead geometry · Microstructure · Submerged arc welding

## 1 Introduction

The submerged arc welding (SAW) is a versatile and efficient joining process and finds applications in pressure vessel manufacture, large pipe fabrication, structural applications, ship building, bridge construction, welding applications in automotive industry, repair work and surfacing and general-purpose fabrication of thick plates, since the process allows for high deposition rate and deeper penetration. Also the process can be fully automated, thereby enhancing productivity [10]. The unique advantage of SAW is its capability to join plates of medium to higher thickness with a single pass or minimum number of multiple passes. In fabrication works, weld procedures and weld process variables play a significant role in attaining weld quality which

is important as it determines the life of the components in service and prevents unexpected failures. The understanding of process variables and their effects on overall weld quality is prerequisite to select the optimum welding variables for achieving high productivity and without compromising on reliability of fabrication. Yang et al. [32] conducted BOP experiments on ASTM A36 grade steel of 19-mm-thick plates that larger bead width is influenced by voltage and smaller electrode extension and also developed regression mathematical equations for predicting bead width. Chandel et al. [5] theoretically related the welding variables to resultant bead geometry in SAW of mild steel plates and concluded electrode diameter does not influence the weld quality. Gowrisankar et al. [8] fabricated 316L hot-rolled stainless of 25 mm thickness using multiple-pass SAW and found it was observed that proportion of delta ferrite at root and surface varies significantly with number of passes. Piatti and Vedani [25, 26] fabricated 316 stainless steel of 50 mm thickness with double-‘U’ groove geometry with 28 weld passes and observed variation in ferrite content and its morphology across the weld geometry, which are due to the multiple thermal cycles experienced by the material. Also the tensile strength of the deposited weld metal is lower to

---

Technical Editor: Lincoln Cardoso Brandao.

---

✉ P. V. S. S. Sridhar  
p.sridhar@iitg.ac.in

<sup>1</sup> Department of Mechanical Engineering, Indian Institute of Technology Guwahati, North Guwahati, Assam 781 039, India

that of solution-annealed weld metal. Gunaraj and Murugan [9] developed a mathematical equation for calculating bead parameters for a bead on plate geometry. It was concluded that final bead geometry is a result of direct and interaction effects of welding variables. Prasad and Dwivedi [27] study reveals that SA welding traverse speed has profound effect on weld metal toughness in HSLA steels. Their study concluded that higher toughness was obtained at low traverse speeds when compared with higher ones. Kiran et al. [12] studied weld bead profile for tandem SAW of HSLA steels. The effect of leading current and trailing current on reinforcement height, penetration and weld width was analyzed using response surface methodology. It can be derived from their study that leading current influences penetration, while reinforcement height and penetration were affected by trailing current. Mahapatra et al. [19] developed 3D finite element model to forecast temperature distributions and distortions for double-sided SAW process incorporating the effect of filler deposition and weld reinforcements in the heat source model on mild steel plates of 12 mm thickness, and they observed good correlation between experimental and numerical results. Biswas et al. [4] developed a heat source model for estimating the thermal history and distortions in a double-sided fillet joint and was found the angular distortions and peak temperatures predicted were well matched with experimentally achieved results. Mondal et al. [21] and Pandey et al. [23] studied angular deformation of fillet welds produced by submerged arc welding and found that welds made by single-sided welding and welding direction have pronounced effect angular distortion. Toma et al. [30] conducted experiments on series 304 austenitic steel using direct current (+ve) and alternating square wave current for 25-mm-thick plates with neutral flux and chromium compensating flux and found that CVN impact specimens at cryogenic temperatures broke in ductile fashion and best results on test were obtained with AC square wave and neutral flux. Amanie et al. [1] fabricated SA516 grade 70 steel and observed that welding speed has more impact than current in attaining final weld microstructure which comprises of acicular ferrite and Widmanstätten ferrite. Shen et al. [28] welded ASTM A709 grade 50 steel plates and compared the effect of heat input on bead morphology between single-wire and double-wire SAW. Interestingly, the bead contact angle was decreased linearly with the increase in the heat input. Luo et al. [17, 18] joined 2205 duplex stainless steel with double-‘V’ groove geometry and observed secondary phases are clustered in the middle of the fusion zone as a result of post-welded heat treatment (PWHT). The high values of microhardness are normalized along fusion zone and heat-affected zone (HAZ) after PWHT. Arya et al. [2] investigated the effect of different plate thicknesses and cooling rates on microstructure and mechanical properties of SA 516 grade 60 pressure vessel steel welded using submerged arc

welding. It is established that plates with higher thickness with same heat input resulted in better impact strength to that of thinner plates. Chowdhury et al. [7] evaluated weld bead characteristics, mechanical and microstructural aspects in Ti–6Al–4V alloy welded with electron beam welding. It is found that weld bead characteristics and grain size are governed by power density for a given energy conditions. Choudhary et al. [6] carried out bead on plate experiments to study the effect of direct and indirect weld input parameters on weld width, reinforcement and penetration in submerged arc welding of AISI 1023 steel. The effects were studied by means of genetic algorithm, Jaya algorithm and desirability approach. It is found that Jaya algorithm yielded better optimization results as compared with other approaches. From the detailed study of the published literature, even though the austenitic stainless steels (SS 304) have strengths equivalent to that of mild steels and possess good ductility, corrosion resistance and toughness they were sparsely explored by submerged arc welding.

The weld quality and reliability is very much important in fabrication of critical components, namely boilers, headers and steam piping's in power plants, petrochemical and nuclear reactor components, where 300 grade stainless steels find wide applications [29]. The austenitic stainless steels possess low thermal conductivity and high coefficient of thermal expansion than mild steels; hence, they are more subjected to distortion. The welded component distortion has serious implications as it alters the overall dimensions of the fabricated structure. Also weld distortion is inevitable, and hence, it should be kept minimum. For assembly of medium to thick plates without edge preparation, the double-sided SAW is economical and efficient production process, for manufacturing structures with minimum distortion. It is noticed that very few published literatures were available on DSSAW of SS 304 austenitic stainless steel, in spite of the important industrial applications. The present investigation focuses on effect of weld process parameters on bead geometry, fusion zone profile and mechanical properties for DSSAW of 8-mm-thick austenitic stainless steel. To demonstrate advantage of DSSAW over single-sided SAW, a comparative study on mechanical properties and angular distortion is also reported in this work.

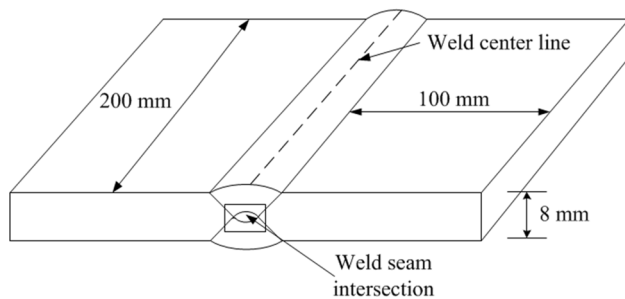
## 2 Experimental investigation

### 2.1 Materials

ASTM A 240 grade 304 austenitic stainless steel of dimensions  $200 \times 100 \times 8$  mm was cut from a rolled sheet. The solid welding electrode of 3.2 mm diameter (308L SS) conforming to AWS/SFA 5.9 was used as filler material. An agglomerated neutral chromium compensating flux ESAB

**Table 1** Chemical composition of SS 304 (wt%)

C	Mn	Si	Cr	Ni	Ph	S	Al	Co
0.024	1.89	0.59	18.91	8.43	0.017	0.011	0.011	0.093
Cu	Nb	Ti	V	Pb	Sn	Fe		
0.478	0.052	0.041	0.045	0.014	0.02	Bal.		

**Fig. 1** Schematic illustration of double-sided SAW specimen

OK 10.92L (EN 760 SACS2Cr DC) with basicity index of 0.88 was used in the study. The grain size of flux ranges between 0.2 and 1.6 mm. The chemical composition of the base material [31] used in the present investigation is given in Table 1.

## 2.2 Welding procedure

The workpieces were segmented by wire EDM, and subsequently, the contamination affected by the coolant was removed with a chemical agent. While wire EDM is cut, the temperature rise in the workpieces is negligible; hence, prior HAZ formation on the edges was circumvented giving rise to good outcome of weld properties. To hold the plates and to maintain a uniform root gap during SA welding, plates were initially tack welded on both sides and edges. The root gap in square butt welds is set in order to facilitate the passage of molten filler metal from top of workpiece to root of the weld. In the present investigation, root gap was fixed as 2.5 mm. The agglomerated flux used in the present study was reheated to 300 °C for 2 h to exclude of any residual moisture. The welding operation is performed with constant

current setting with reverse polarity. Figure 1 shows the schematic of DSSAW sample.

In double-sided SAW, it is desirable to achieve to 60 to 70% of penetration depth of the base metal thickness in each pass for attaining suitable joint strength [24]. In order to achieve this trial run, experiments were conducted to determine the allowable range of welding parameters for joining the material. Proper control of welding parameters is very much necessary to achieve desired weld quality. The operating variables used in the current study are welding current, voltage and welding speed. Throughout this investigation, the length of stick out was held constant for all welding variables. The experimental process variables are detailed in Table 2.

For comparison between single- and double-sided butt welding, the single-sided welding was also carried out in 8-mm-thick plate with welding current 410 A, voltage 24 V, traverse speed 5.55 mm/s and length of stick out 25 mm.

## 2.3 Bead geometry and microstructure

For studying bead geometry and microstructure, the starting and end portion of the weld plates were discarded as there is a probability of occurrence of defects in that region. All the welded specimens were visually examined for surface defects, like burns and uneven reinforcements, and two samples were transversely extracted at random locations from the welded plate to measure bead geometry and microstructure. They were cut by wire electric discharge machine (WEDM) operated at slow speeds. The metallurgical samples were grinded with SiC emery papers in the increasing order of grit numbers. For attaining mirror finish, further these samples were polished with 0.3 μm alumina suspension applied on a velvet cloth. The etchants are used to reveal the microstructure of the polished

**Table 2** Experimental process variables

Exp.	Joining method	Welding current (A)	Welding speed (mm/s)	Voltage (V)	Length of stick out (mm)
1	Square butt	340/365/390	7.083	24	25
2	Square butt	365	7.083	22/24/26	25
3	Square butt	365	6.8/7.08/7.36	24	25

samples. In present work, samples were etched with glycergia (3:2:1::glycerol:HCl:HNO<sub>3</sub>) solution. The metallurgical structure is examined with Carl Zeiss upright optical microscope interfaced with AXIOVISION software. The macrostructure was studied using Nikon SMZ25 Stereomicroscope. For measurement of bead profiles, the digital images were imported into imaging software followed by calibration and measurement. The bead width is the uncovered surface of a weld on the side from which the welding is performed.

The bead width is measured on top width of the fusion zone. The weld penetration is the depth of a groove weld which stretches out into the base of a joint and is estimated on the centerline of root cross-sectional area.

The reinforcement is characterized as excess weld metal from upper surface of the workpiece. The bead nomenclature for double-sided SAW is illustrated in Fig. 2.

The plates were joined with same heat input, i.e., same welding parameters on both sides. Hence, weld bead profile parameters such as bead width ( $b_w$ ), reinforcement height ( $r_h$ ), penetration area ( $p_a$ ), reinforcement area ( $r_a$ ) and depth of penetration ( $p_d$ ) were measured for single side, i.e., 2nd weld pass. In the present investigation, two samples were sectioned from appropriate locations of each welded plate for measuring the weld bead parameters.

### 2.4 Measurement of angular distortion

The welding distortion in a simple butt joint is measured with coordinate measuring machine (Make: Carl Zeiss, USA). Figure 3a shows angular measurement setup using CMM (b) schematic of sample with measuring points.

The workpiece under observation was placed on a V Block and is positioned on the horizontal bed of the machine. With the help of trisquare, straight lines are scribed on the top face of the specimen. The control points for measurement were marked with the help of center punch. The coordinate measurement machine is interfaced with U-Soft software. The included angle between the two collinear lines is measured. Two reading were taken transversely: one at the top edge and other at center of the welded sample. The distorted angle is measured using the formula:

$$\theta = \frac{(180 - \beta)}{2} \tag{1}$$

where  $\beta$ =included angle of the welded sample in degrees and  $\theta$ =angle of distortion in degrees.

### 2.5 Uniaxial tensile test

Two samples along transverse direction of weld were cut from each plate to find the tensile properties of the DSSAW

Fig. 2 Nomenclature of the weld bead with root gap for DSSAW

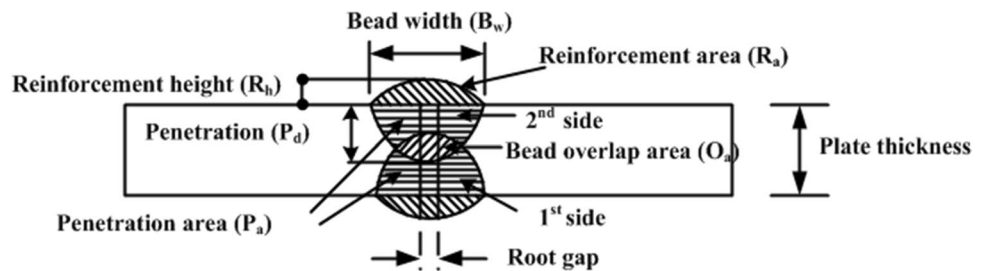
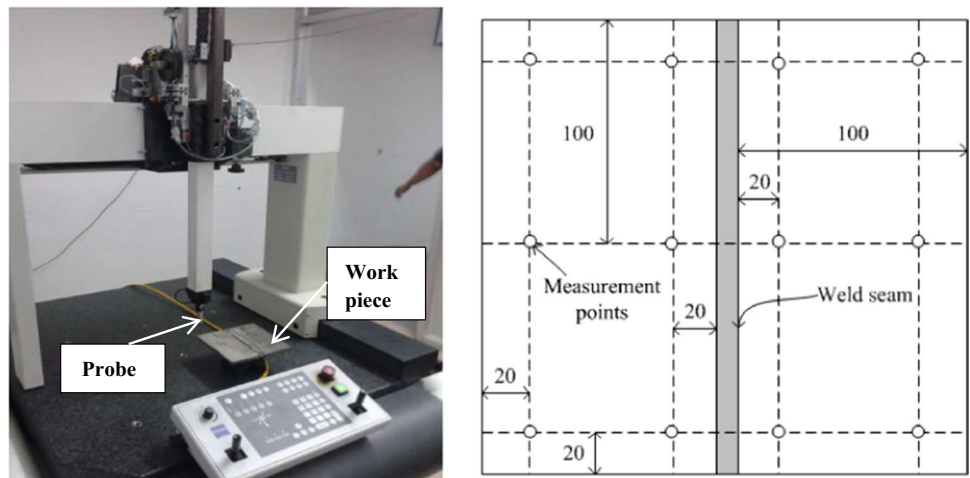


Fig. 3 a Measurement of angular distortion with coordinate measuring machine (CMM), b schematic of sample with measuring points



welded sample. The tensile samples were prepared as per (ASTM E8/E8M [3]). The universal testing machine (INSTRON 8801) is interfaced with a pc and operated with a crosshead speed of 1 mm/min. The schematic representation of the tensile sample is shown in Fig. 4.

### 3 Results and discussion

#### 3.1 Weld macrostructure

Generally, welded joints are prone to cracks, microporosities, slag inclusions and incomplete penetration. Therefore, it is required to ensure that no such weld defects arise while performing the experiments. All weld samples are visually inspected, before proceeding to further characterization. For all process variable combinations, no such defects were detected. Figure 5 shows the macrostructures of the Exp. Nos. 2, 3, 6 and 7, respectively. Also, Fig. 5 represents the fusion zone profile for a common parameter used in Exp. Nos. 2, 5 and 8. The present investigation is carried out by

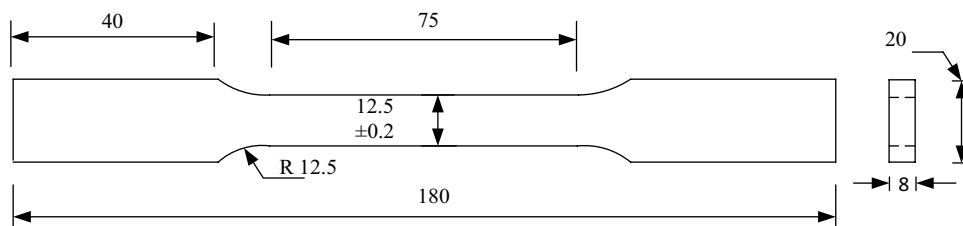
varying the process variables, namely current, speed and voltage.

#### 3.1.1 Weld microstructure

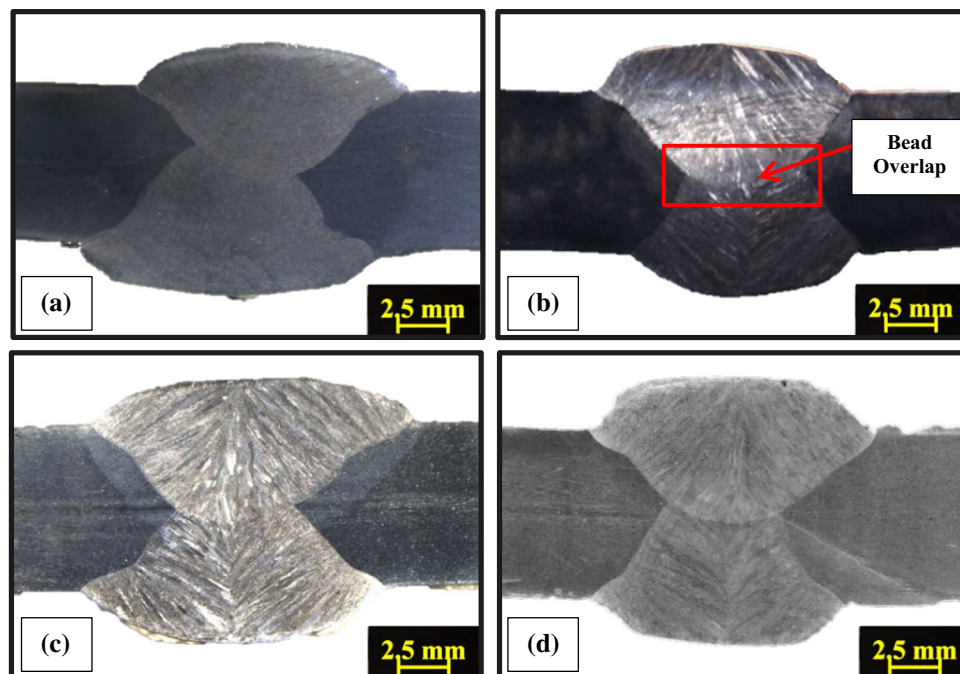
Figure 6 shows the microstructure of the as-received base metal.

The microstructure of as-received AISI 304 stainless steel consists of equiaxed austenite grains and deformation twins that were formed during thermomechanical processing. The microstructure of weld metal consists of columnar dendritic grains of delta ferrite and in a matrix of austenite with no sign of equiaxed grains. This is due to fact that the temperature gradient within the weld pool is steep. Since submerged arc welding is basically used for joining thicker plates, large heat is input into the material and large weld pool is formed. The rate of cooling is slower due to flux cover the whole weld pool, which results in low crystallization rate. In order to get equiaxed grains, high cooling rates are desirable. The dendritic crystal grows perpendicular to fusion line and intersects in the midregion of the weld pool. Figure 7 shows the interface zone between fusion zone and HAZ.

**Fig. 4** Schematic of representation of tensile sample [3]. All dimensions are in mm



**Fig. 5** As-polished macrostructure: **a** Exp. Nos. 2, 5 and 8 (common parameter). Etched macrostructures of **b** current variation Exp. No. 3; **c** voltage variation Exp. No. 6; **d** speed variation Exp. No. 7



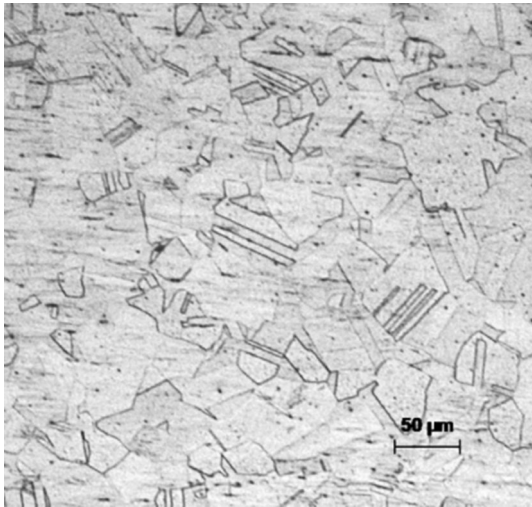


Fig. 6 Microstructure of base metal AISI 304

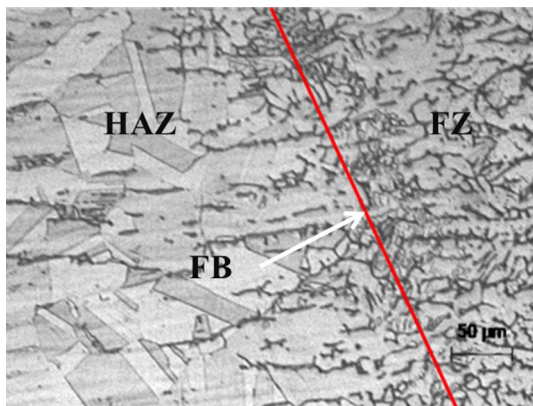


Fig. 7 Fusion zone and HAZ interface

Due to segregations of alloying elements in the weld pool and non-spontaneous nucleation, refinements of dendritic grains were seen. Hence, relatively smaller dendrites were seen in the fusion zone.

The microstructure in the vicinity of the weld zone equiaxed grains of austenite was observed. The solidification of weld pool is a dynamic mechanism with epitaxial growth of crystals and variations in the temperature gradient within the weld pool and different growth rates of crystals. In weld solidification mechanics, important parameters that affect the microstructure are temperature gradient within the weld pool ( $G$ ), growth rate ( $R$ ) and degree of undercooling ( $\Delta T$ ) and alloy composition ( $C_0$ ) [14]. All these parameters essentially vary from location to location and also differ with different welding processes and welding conditions. This microstructure of weld pool diverges from location to location within the fusion zone. Two types of morphology of delta ferrite are observed within the weld metal shown in Figs. 8 and 9. The evolution of the microstructure in the weld zone depends on mode of solidification of the stainless steel.

The white portions in the microstructure correspond to austenite, and the darker portions are delta ferrite. Figure 8 shows that the morphology of delta ferrite varies from lathy ferrite to skeletal ferrite in the fusion zone.

The intersection region of the weld passes shown in Fig. 9 wherein on the one side skeletal delta ferrite is observed, which is the second pass. Similar types of morphologies of delta ferrite were observed in all regions of all the weld samples. These types of occurrences are due to the different thermal cycles and cooling rates within the weld zone [20]. It can also be articulated that at regions of adequate cooling rates, skeletal delta morphology has been formed. Figure 10 shows the skeletal morphology of delta ferrite at midportion in the fusion region, where cooling rates were moderate.

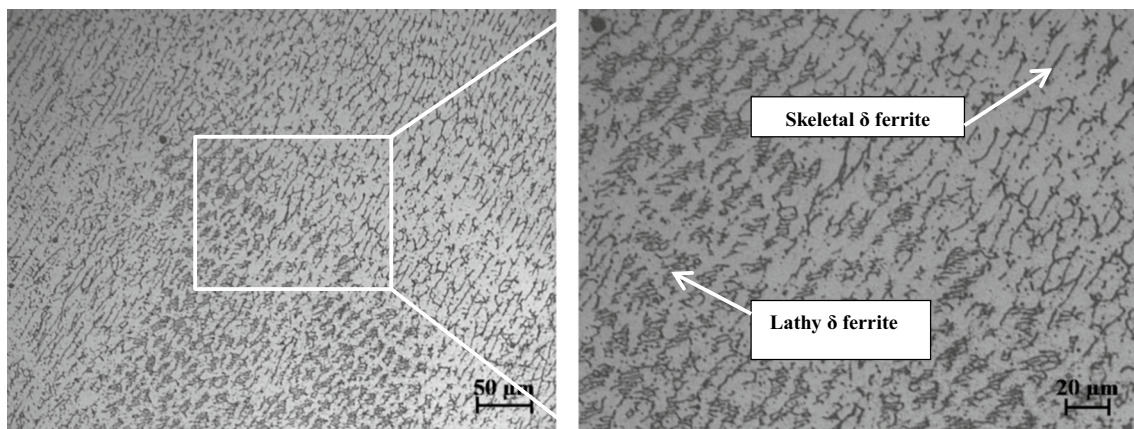
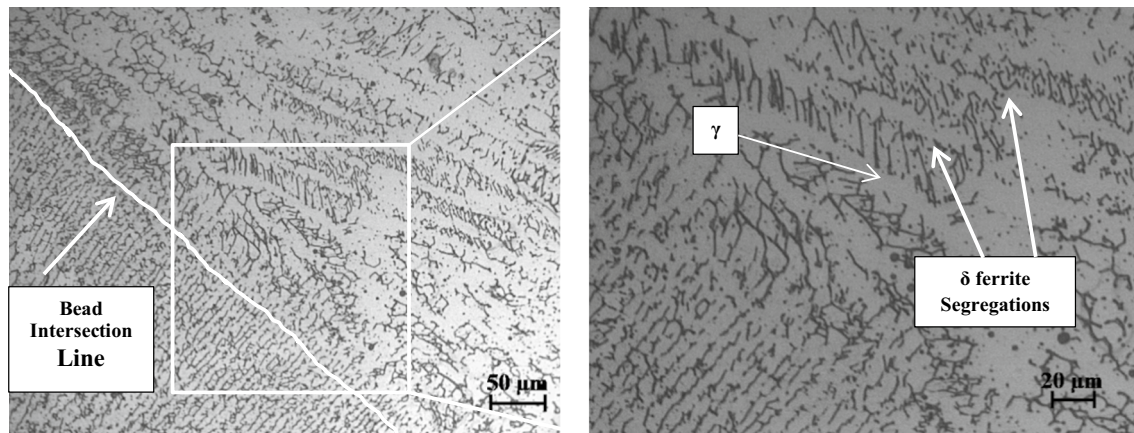
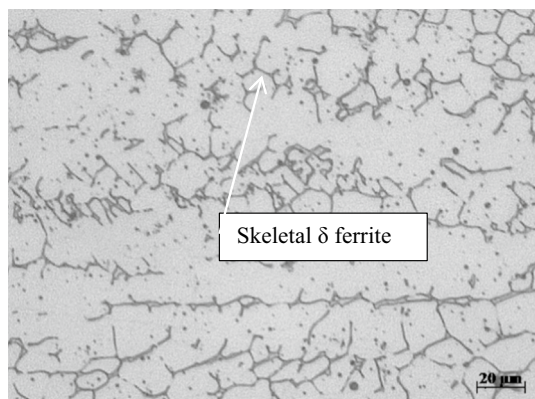


Fig. 8 Microstructure of weld zone in the upper midregion for Exp. No. 3



**Fig. 9** Microstructure of weld zone intersection of top and bottom pass in the for Exp. No. 3



**Fig. 10** Skeletal morphology of delta ferrite at fusion zone for Exp. No. 3

This is a result of prior consumption ferrite into austenite matrix, since ferrite is sufficiently enriched with ferrite promoting agents like chromium and depletion of austenite stimulating agents such as nickel, which is stable at ambient temperature, where there is no diffusion. In regions where cooling rates are high, lathy delta ferrite is formed which is due to limited diffusion during ferrite–austenite transformation [16]. As the diffusion distance is low, there will be a decrease in concentration gradient, which enhances the phase transformation efficiently; therefore, spacing is less between laths [20]. In austenitic stainless steels, certain quantity of delta ferrite phase is desirable as it prevents weld from hot cracking [13, 16].

### 3.2 Effect of process variables on fusion zone profile

In this work, the individual effect of each process variable is studied, while keeping all other parameters constant. The

average results of two samples were considered for analyzing the fusion zone profile. The relation between penetration and welding current, traverse speed and voltage is defined by welding technique performance factor (WTPF) [11], given as

$$\text{WTPF} = \sqrt[3]{\frac{I^4}{SV^2}} \quad (2)$$

where  $I$  = welding current (A),  $S$  = traverse speed (mm/s) and  $V$  = welding voltage (volts).

#### 3.2.1 Effect of welding current

Figure 11a–c depicts the effect of welding current on bead width, reinforcement height, reinforcement area, penetration area, penetration depth and bead overlap area. Also Fig. 11d shows the relationship between welding technique performance factor and penetration depth with variation in welding current.

Figure 11a–d shows that weld bead parameters, namely  $B_w$ ,  $R_h$ ,  $P_a$ ,  $R_a$ ,  $P_d$  and  $O_a$ , generally increased with the increase in the welding current from 340 to 390 A. Figure 11a shows that weld width increases initially, and after that, it reduces slightly, with further increase in current, but is higher than the initial weld width. Figure 11b shows that as welding current increases, the reinforcement area and penetration area gradually increase. The welding current is the most crucial process variable in submerged arc welding (SAW). The amount of heat generated during the welding process is directly proportional to the square of the welding current. Figure 11c shows that penetration depth increased linearly with an increase in welding current since the welding current has a pronounced effect on the depth of penetration. According to Murugan and Gunaraj [22], the effect of welding can be explained as follows: The welding current

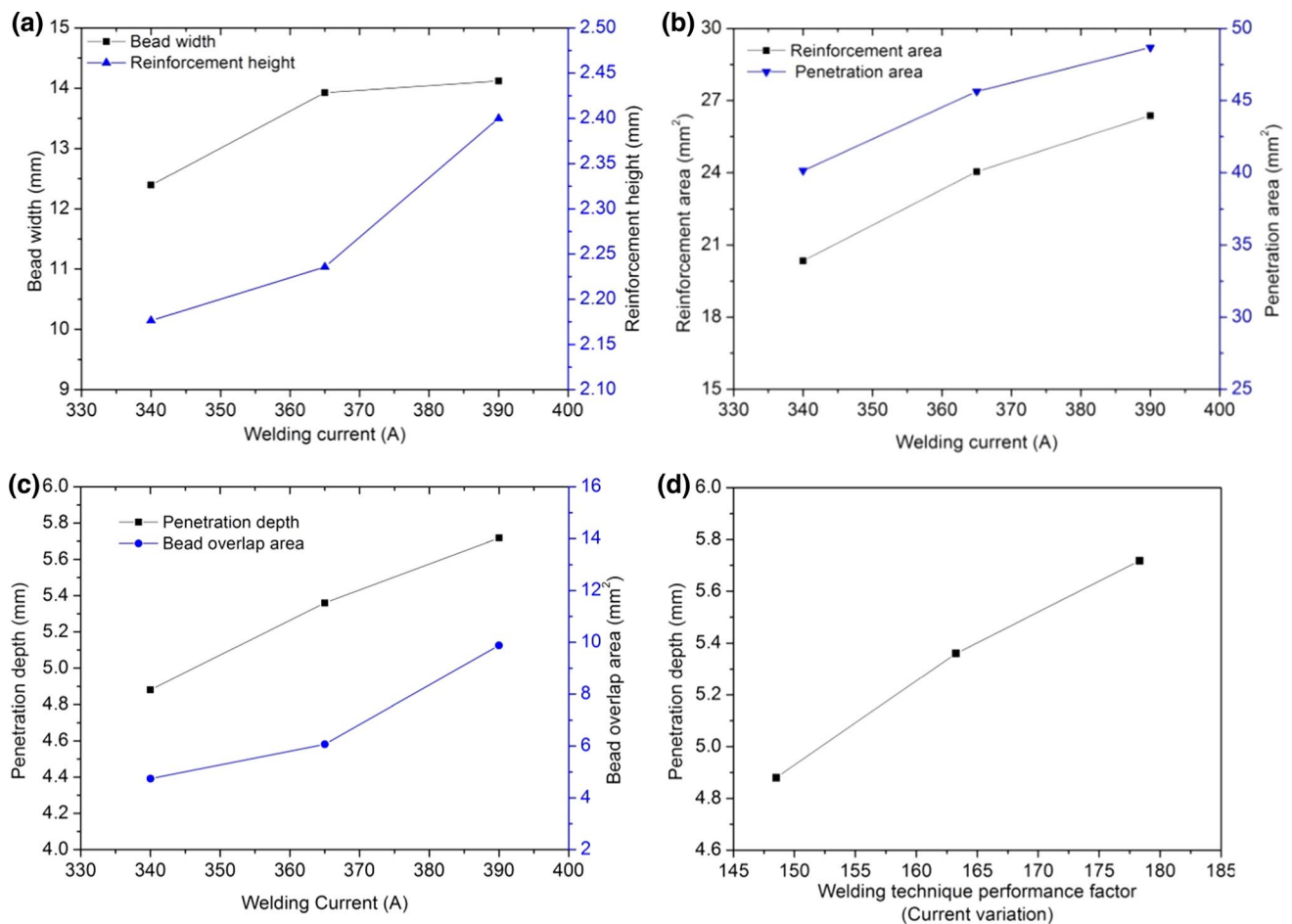


**Fig. 11** Effect of welding current on: **a** bead width and reinforcement height; **b** reinforcement area and penetration area; **c** penetration depth and bead overlap area; **d** welding technique performance factor and penetration depth

increases the momentum of filler metal droplets, and these impinge the weld pool causing deep penetration. Keeping all parameters constant and increasing the welding current enhance the penetration, electrode deposition rate, bead width and weld cross-sectional area. Also, it can be noticed that bead overlap area increases as welding current is varied from 340 to 390 A, which is due to higher heat generation and larger fusion zone size at increased welding currents. Some aspects of Fig. 11 need more description. The welding technique performance factor (WTPF), which is related to penetration depth, is shown in Fig. 11d. It can be observed that an increase in welding current is directly proportional to WTPF; hence, it follows the same trend as that of  $P_d$ .

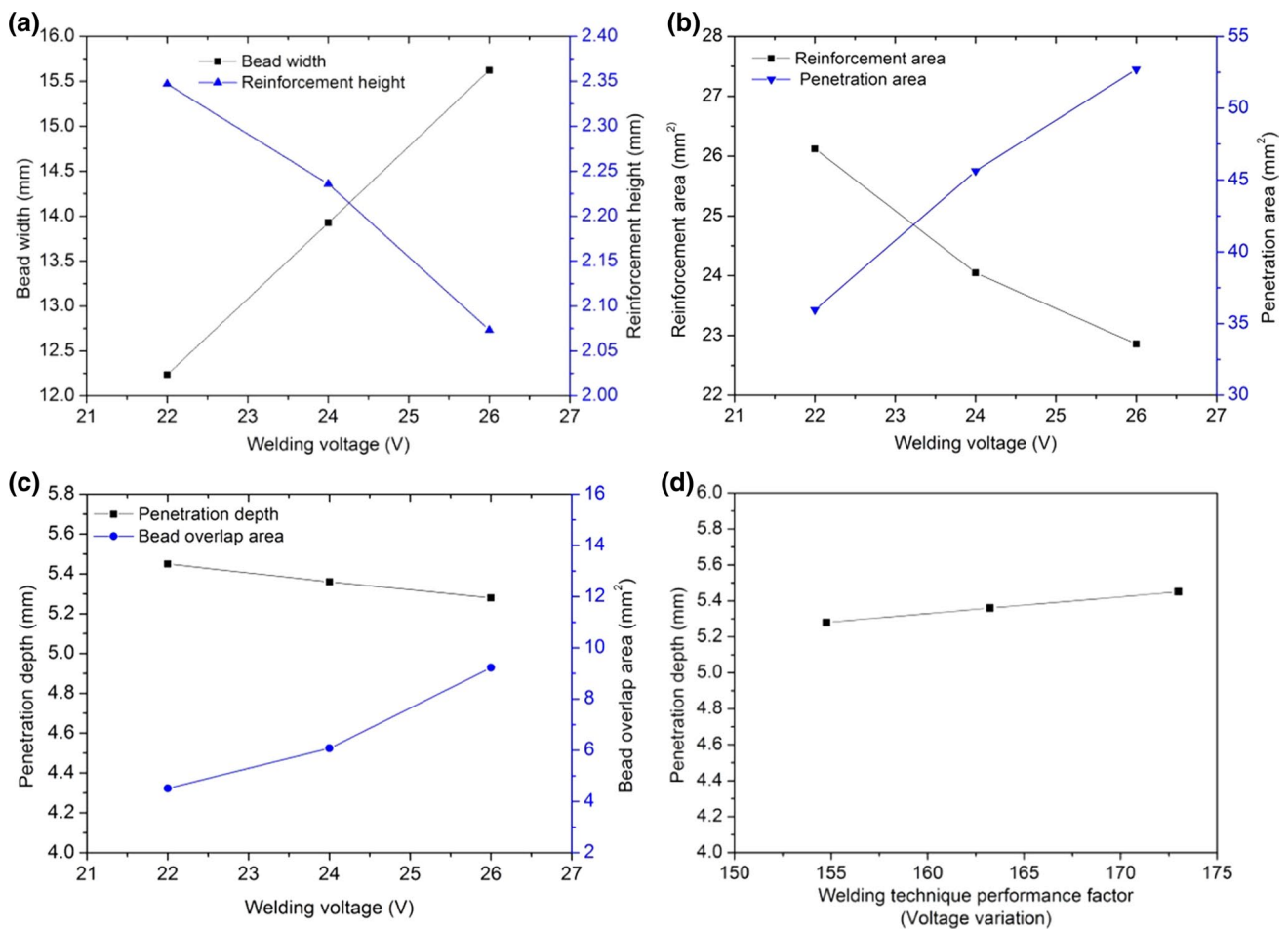
### 3.2.2 Effect of welding voltage

Figure 12a–c depicts the effect of welding voltage on bead width, reinforcement height, reinforcement area, penetration area, penetration depth and bead overlap area. Also Fig. 12d shows the relationship between welding technique

performance factor and penetration depth with variation in welding voltage.

The welding voltage is the electrical potential difference between the tip of the filler wire and the surface of the molten weld puddle. Figure 12a shows that an increase in welding voltage from 22 to 26 V, while keeping all other parameters constant, has resulted in a steady increase in weld bead width. The increase in voltage increases the arc length, hence more melting at the surface due to large arc spread, which increases weld width. The welding voltage has a direct effect on the shape of the fusion zone profile and external bead appearance. The increase in the voltage results in flatter bead, and hence, reinforcement height reduces with the increase in the welding voltage. Figure 12b shows that the reinforcement area decreases with an increase in voltage and penetration area increases. The increase in penetration area attributes to the widening of the weld pool at the expense of penetration depth. Figure 12a and b shows that reinforcement height and area were reduced with an increase in voltage, as welding





**Fig. 12** Effect of welding voltage on: **a** bead width and reinforcement height; **b** reinforcement area and penetration area; **c** penetration depth and bead overlap area; **d** welding technique performance factor and penetration depth

voltage does not appreciably affect the electrode melting rate, hence lower filler material deposition.

Figure 12c shows that as the voltage is increased from 22 to 26 V, there is a slight reduction in the depth of penetration. The increase ( $P_d$ ) in low voltages is attributed to flow of heat in the thickness direction and smaller arc length, which causes a positive effect on penetration depth and more reinforcement height. It can be concluded that the effect of welding voltage on penetration is only marginal. Also, as the voltage is increased from 22 to 26 V bead overlap area increases and this is due to the increase in the penetration area at a higher voltage. Figure 12d shows the WTPF increases with a decrease in welding voltage. It can be concluded that as WTPF reduces, the penetration depth ( $P_d$ ) also reduces.

### 3.2.3 Effect of Traverse speed

Figure 13a–c depicts the effect of traverse speed on bead width, reinforcement height, reinforcement area, penetration area, penetration depth and bead overlap area. Also

Fig. 13d shows the relationship between welding technique performance factor and penetration depth with variation in traverse speed.

Figure 13a shows the effect of traverse speed on bead width and reinforcement height. Figure 13a shows that bead width and reinforcement height decrease with the increase in the traverse speed. This reduction is because heat input applied per unit length into the joint decreases with the increase in the traverse speed, and hence, lesser filler metal is deposited, which leads to smaller weld bead and less reinforcement height. It can be concluded that traverse speed has an inverse effect on bead width and reinforcement height. Figure 13b shows that with the increase in the traverse speed both reinforcement area and penetration area reduce, which is due to less time the base metal had exposed to the heat of welding arc. Figure 13c shows that as traverse speed increases, penetration and bead overlap area were reduced. It is observed that at lower traverse speed, i.e., 6.8 mm/s the higher depth of penetration of 5.54 mm was noticed, while other operating parameters were held constant. Figure 13d

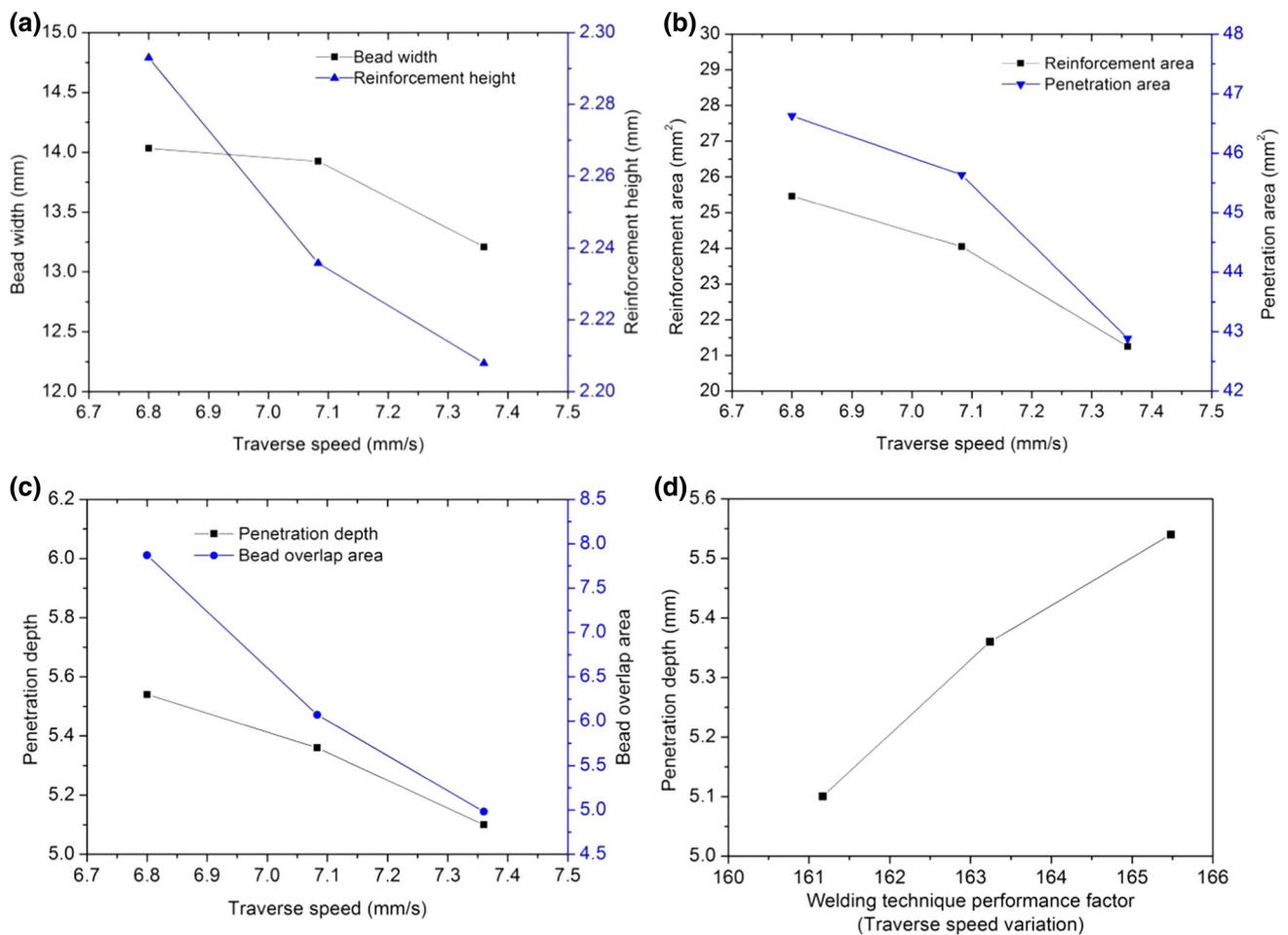


**Fig. 13** Effect of traverse speed on: **a** bead width and reinforcement height; **b** reinforcement area and penetration area; **c** penetration depth and bead overlap area; **d** welding technique performance factor and penetration depth

shows that as traverse speed increases, WTPF starts to reduce, and hence, the depth of penetration also is found to be reduced. The average results of the weld bead and fusion zone analysis are shown in Table 3.

In the parameter set, experiment '2' is included in all the three parameter variations. Hence, the results of Exp. No. 2, 5 and 8\* are same.

### 3.3 Effect of process parameters on tensile properties

The resistance offered by a material against fracture is termed as tensile strength. The tensile test is carried out under standard test procedures as described in ASTM E8M standards. The test is performed at room temperature, i.e., 23 °C. The average base material (BM) UTS is 714.16 MPa, YS is 302.9 MPa, and elongation is 54.57%. The results of the tensile test are shown in Table 4. Figure 14 a–c shows the influence of individual welding parameters, namely current, voltage and traverse speed, on tensile strength (UTS) and

yield strength (YS), respectively. The UTS of the welded joint ranged from 570.44 to 669.13 MPa, while YS ranges from 253.43 to 284.89 MPa. Figure 14a shows that tensile strength and yield strength increase with the increase in the welding current and attain the peak value. It can be inferred that welding current has profound influence on mechanical properties of a welded joint. Similarly, Fig. 14b shows that as welding voltage increases, tensile strength and yield strength also tend to increase, after which we can observe there is a decreasing trend in tensile properties. Figure 14c shows that as traverse speed increases tensile properties are found to be reduced. This is due to the fact that the rate of heat input per unit length is reduced at increased speeds which lead to smaller fusion zone size. The traverse speed is important parameter from productivity point of view in a welding process.

The traverse speed cannot be set very low as it may cause material degradation due to overexposure to arc heat and can cause overdeposition. Hence, traverse speed is not a desirable parameter for control of mechanical properties.

**Table 3** Results of effect of process variables on fusion zone profile

Parameter set	$B_w$ (mm)	$R_H$ (mm)	$P_d$ (mm)	$R_a$ (mm <sup>2</sup> )	$P_a$ (mm <sup>2</sup> )	$O_a$ (mm <sup>2</sup> )	WTPF
<i>Welding current variation</i>							
Exp. No. 1	12.39	2.18	4.88	20.34	40.15	4.74	148.51
Exp. No. 2	13.93	2.24	5.36	24.05	45.63	6.07	163.24
Exp. No. 3	14.12	2.40	5.72	26.37	48.68	9.88	178.32
<i>Welding voltage variation</i>							
Exp. No. 4	12.23	2.35	5.45	26.12	35.96	4.51	172.99
Exp. No. 5	13.93	2.24	5.36	24.05	45.63	6.07	163.24
Exp. No. 6	15.62	2.07	5.28	22.86	52.7	9.22	154.76
<i>Traverse speed variation</i>							
Exp. No. 7	14.03	2.29	5.54	25.46	46.63	7.87	165.48
Exp. No. 8	13.93	2.24	5.36	24.05	45.63	6.07	163.24
Exp. No. 9	13.21	2.21	5.10	21.25	42.89	4.98	161.17

**Table 4** Experimentwise tensile properties

Parameter set	Tensile strength (MPa)	Yield strength (MPa)	% Elongation	% TS of BM	% YS of BM
<i>Welding current variation</i>					
Exp. No. 1	633.90	274.02	70.51	88.76	90.47
Exp. No. 2	660.32	277.09	76.49	92.46	91.48
Exp. No. 3	669.13	284.89	74.00	93.70	94.05
<i>Voltage variation</i>					
Exp. No. 4	570.44	253.43	65.20	79.88	83.67
Exp. No. 5	660.32	277.09	76.49	92.46	91.48
Exp. No. 6	653.42	281.51	81.99	91.50	92.94
<i>Traverse speed variation</i>					
Exp. No. 7	648.25	276.20	81.75	90.77	91.18
Exp. No. 8	660.32	277.09	76.49	92.46	91.48
Exp. No. 9	644.22	273.55	78.19	90.21	90.31

For understanding the mode of failure in the tensile specimen, the fracture surface of the tensile specimen is examined under high-resolution FESEM. The failure of the welded joint occurred from the weld region for all the DSSAW samples.

Figure 15 shows the fracture surface of the tensile sample for Exp. No. 4. It is observed that the fracture was ductile in nature, with equiaxed dimples distributed non-homogeneously over the fracture surface, which indicates that material has sufficiently undergone plastic flow before failure. The fracture surface of the dimple rupture comprises peaks and valleys. The dimple rupture mode fracture is associated with nucleation of voids at the inclusions in the material [15]. In general, the deeper the dimples, the better is the ability of the material to undergo plasticity before failure.

### 3.3.1 Percentage elongation

Figure 16a shows the comparison of the percentage of elongation between single-sided weld, double-sided weld and

base material. Figure 16b shows the enhancement of percentage of elongation with that of base material. The percentage of elongation of DS-SAW (Exp. No. 3) is compared with single-sided SAW (SS-SAW) and base material in this session.

It is observed that the percentage of elongation is higher for double-sided SAW (74%), when compared with that of the base metal (55.52%) and single-sided sample (26.4%). This higher percentage elongation can be due to the additional heat input that is used to fuse the joint from the other side as it can cause some annealing like effect on the welded joint and this results in enhanced percentage of elongation in case of double-sided SA welded sample. Figure 16b shows that a maximum of 50.2% enhancement in elongation with that of base material is obtained for Exp. No. 6 in DSSAW and lowest for Exp. No. 4, i.e., 19.48%. The percentage of elongation of all double-sided welded samples has surpassed the percentage of elongation of the base material. From this result, it can be concluded that double-sided welding has effectively retained its ductility of the weld seam.

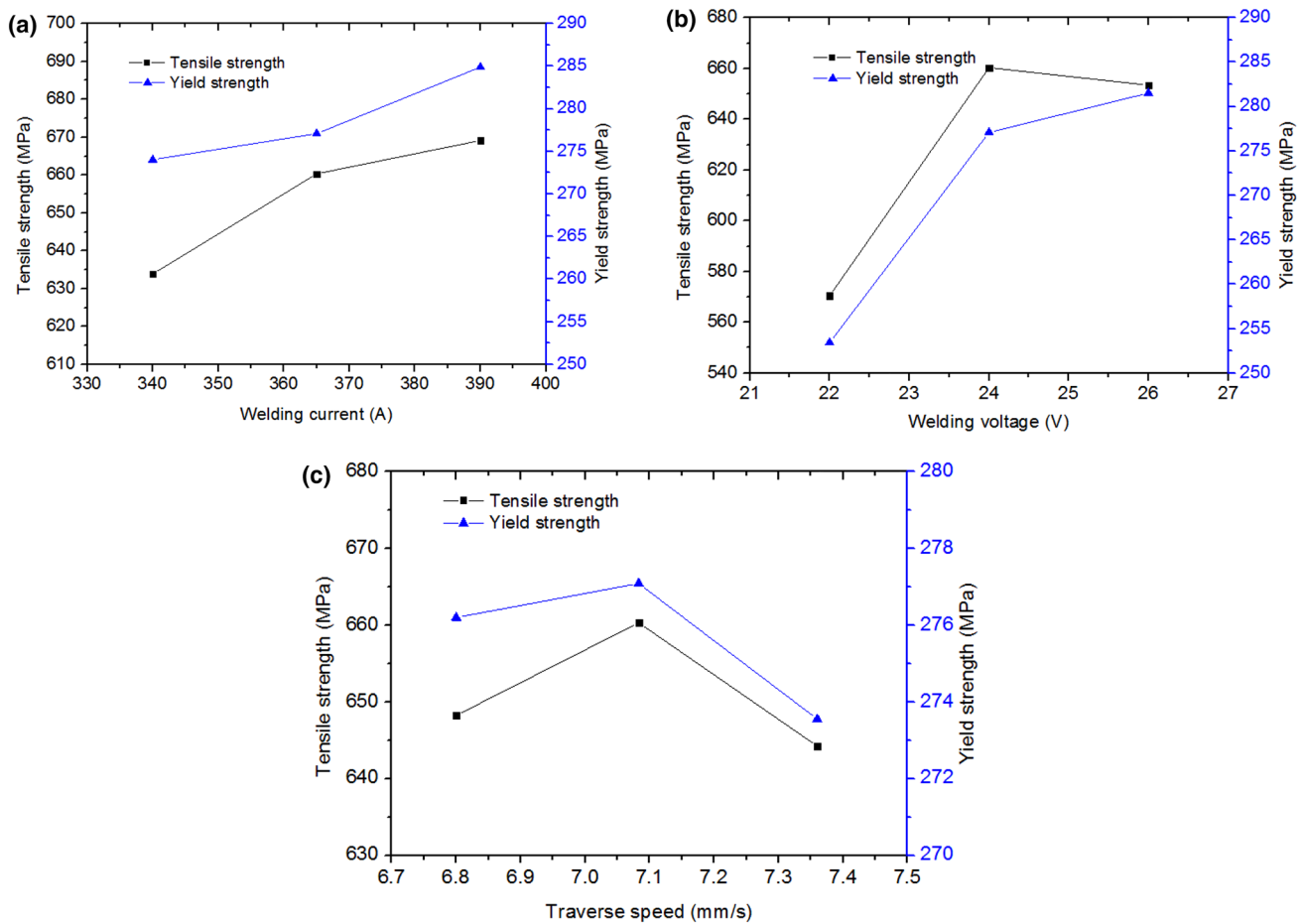


**Fig. 14** Results of uniaxial tensile testing for variation of: **a** welding current; **b** welding voltage; **c** traverse speed

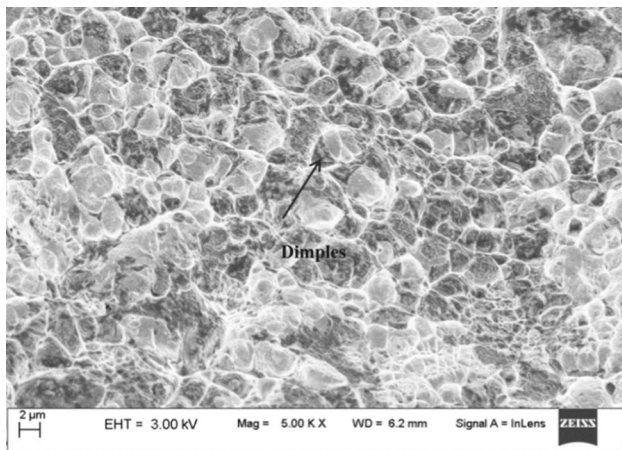
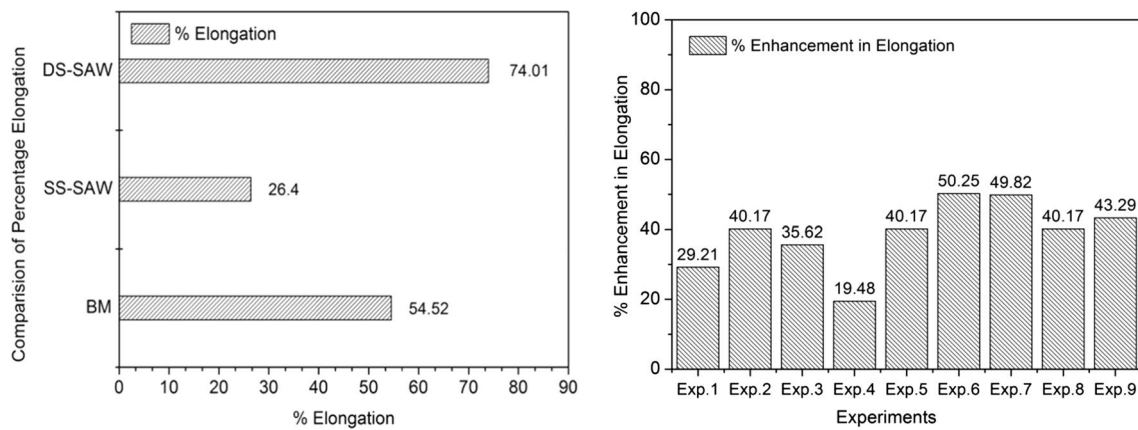


**Fig. 15** Fracture surface of tensile specimen for Exp. No. 4

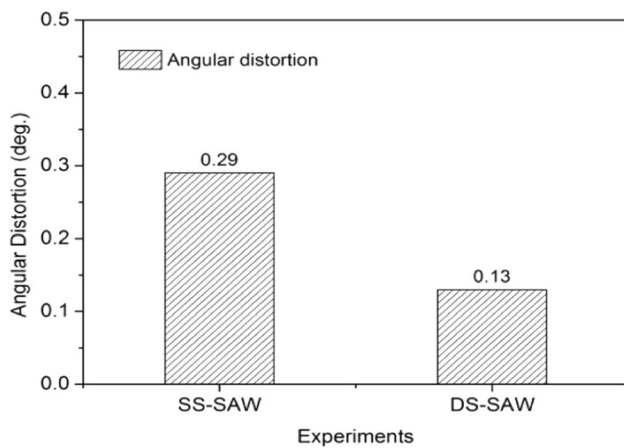
### 3.4 Comparison of angular distortion with single-sided SAW

Figure 17 shows the comparison of average angular distortion between single-sided SAW and double-sided SAW.

The angular distortion of DS-SAW welded sample (Exp. No. 4) joined with nominal heat input is compared with a single-sided SAW. It is observed that the angular distortion obtained for DS-SAW ( $0.13^\circ$ ) is much less than single-sided SAW ( $0.29^\circ$ ). As much as 55.17% reduction in angular distortion with respect of single-sided SAW is gained. In double-sided submerged arc welding, the initial pass produces the bottom reinforcement. The final angular distortion produced after the 2nd pass will be minimal because the bottom bead reinforcement produced in the 1st pass acts as a constraint for the subsequent pass [19]. Hence, double-sided



**Fig. 16** Percentage of elongation. **a** Comparison of percentage of elongation. **b** Percentage enhancement in elongation with that of base metal



**Fig. 17** Comparison of angular distortion between single-sided SAW and double-sided SAW

SAW can be one of the options to control the angular distortion in medium to thick plates.

## 4 Conclusions

In this study, the effect of process variables on bead geometry, mechanical properties and angular distortion of double-sided submerged arc welding of AISI 304 austenitic stainless steel was investigated. The following conclusions are arrived based on this study.

- Conclusions on effect of process variables on bead geometry:
  - As welding current increases, the depth of penetration and bead overlap area found to be enhanced.

Here, the maximum depth of penetration of 5.72 mm and bead overlap area of 9.88 mm<sup>2</sup> are obtained for the current of 390 A.

- Welding voltage found to have a significant influence on bead width ( $B_w$ ) and penetration area ( $P_a$ ). With the increase in the welding voltage, both bead width and penetration area increase. A maximum bead width of 15.62 mm and penetration area of 52.7 mm<sup>2</sup> were obtained for the voltage of 26 V.
- It is clear from the present investigation that as the traverse speed increases, all the bead parameters start to show a declining trend. Hence, it can be concluded that increasing traverse speed results in smaller weld bead and fusion zone profile.

- Conclusions on effect of process variables on tensile properties:

- With an increase in welding current and voltage, the tensile properties are found to be improved, and as speed is increased, tensile properties are found to be reduced. Compared to the other operating parameters, it can be concluded that welding current is the most significant parameter that influences the tensile properties.
- Double-sided SAW effectively improved the ductility of the weld bead. The maximum percentage of elongation of the tensile specimen was significantly enhanced in DSSAW. Highest tensile strength weld sample yielded a percentage of elongation of 74.01%, which is more than the percentage of elongation (54.2%) of the base material. This enhancement is due to some annealing like effect introduced into the fusion zone from the heat input of second weld pass.

- It is found that the percentage reduction in angular distortion with double-sided SAW was around 55.17% as compared to single-sided SAW. Hence, double-sided SAW technique may be advantageous in minimizing angular distortion in butt welds.
- The microstructure of the fusion zone of SS 304 welded samples consists of austenite and dendrites of delta ferrite. The formation of delta ferrite in the fusion zone depends on thermal cycles and cooling rates, and these thermal gradients vary throughout the fusion zone of the weld.

**Acknowledgements** The authors acknowledge the support extended by Department of Mechanical Engineering and Central Instruments Facility, IIT Guwahati, for carrying out this experimental work and characterization studies.

## References

1. Amanie J, Oguocha INA, Yannacopoulos S (2012) Effect of submerged arc welding parameters on microstructure of SA516 steel weld metal. *Can Metall Q* 51:48–57. <https://doi.org/10.1179/000844311X13117643274794>
2. Arya HK, Singh K, Saxena RK (2018) Effect of weld cooling rates on mechanical and metallurgical properties of submerged arc welded pressure vessel steel. *J Press Vessel Technol Trans ASME* 140:1–7. <https://doi.org/10.1115/1.4040274>
3. ASTM E8/E8M (2011) Standard test methods for tension testing of metallic materials. ASTM Int., pp 1–27. <https://doi.org/10.1520/E0008>
4. Biswas P, Mahapatra MM, Mandal NR (2009) Numerical and experimental study on prediction of thermal history and residual deformation of double-sided fillet welding. *Proc IMechE Part B J Eng Manuf* 224:125–134. <https://doi.org/10.1243/09544054JEM1666>
5. Chandel RS, Seow HP, Cheong FL (1997) Effect of increasing deposition rate on the bead geometry of submerged arc welds. *J Mater Process Technol* 72:124–128. [https://doi.org/10.1016/S0924-0136\(97\)00139-8](https://doi.org/10.1016/S0924-0136(97)00139-8)
6. Choudhary A, Kumar M, Unune DR (2019) Experimental investigation and optimization of weld bead characteristics during submerged arc welding of AISI 1023 steel. *Def Technol* 15:72–82. <https://doi.org/10.1016/j.dt.2018.08.004>
7. Chowdhury S, Nirsanametla Y, Muralidhar M, Bag S, Patra SK (2019) Influence of weld parameters on weld regimes and vaporization rate in electron beam welding of Ti6Al4V alloy. *J Br Soc Mech Sci Eng* 41:1–14. <https://doi.org/10.1007/s40430-019-1689-8>
8. Gowrisankar I, Bhaduri AK, Seetharaman V, Verma DDN, Achar DRG (1987) Effect of the number of passes on the structure and properties of submerged arc welds of AISI type 316L stainless steel. *Weld J* 05:147–154
9. Gunaraj V, Murugan N (2000) Prediction and optimization of weld bead volume for the submerged arc process—part 1. *Weld J* 79:286–294
10. Houldcroft PT (1989) P T Houldcroft. Abington Publishing, Cambridge
11. Jackson CE, Shrubbsall AE (1953) Control of penetration and melting ratio with welding technique. *Weld J* 32:172s–178s
12. Kiran DV, Basu B, De A (2012) Influence of process variables on weld bead quality in two wire tandem submerged arc welding of HSLA steel. *J Mater Process Technol* 212:2041–2050. <https://doi.org/10.1016/j.jmatprotec.2012.05.008>
13. Kou S (2003) *Welding metallurgy*, 2nd ed. Wiley, New Jersey. <https://doi.org/10.1103/PhysRevLett.110.075501>
14. Lampman S (1997) *Weld integrity and performance*, 1st edn. ASM International, Materials Park
15. Lippold JC (2015) *Welding metallurgy and weldability*, 1st edn. Wiley, New York
16. Lippold JC, Kotecki DJ (2005) *Welding metallurgy and weldability of stainless steels*. Wiley, New York
17. Luo J, Dong Y, Li L, Wang X (2014) Microstructure of 2205 duplex stainless steel joint in submerged arc welding by post weld heat treatment. *J Manuf Process* 16:144–148. <https://doi.org/10.1016/j.jmapro.2013.06.013>
18. Luo J, Yuan Y, Wang X, Yao Z (2013) Double-sided single-pass submerged arc welding for 2205 duplex stainless steel. *J Mater Eng Perform* 22:2477–2486. <https://doi.org/10.1007/s11665-013-0529-8>
19. Mahapatra MM, Datta GL, Pradhan B, Mandal NR (2008) Modelling of angular distortion of double-pass butt-welded plate. *Proc Inst Mech Eng Part B J Eng Manuf* 222:391–401. <https://doi.org/10.1243/09544054JEM995>
20. Mirshekari GR, Tavakoli E, Atapour M, Sadeghian B (2014) Microstructure and corrosion behavior of multipass gas tungsten arc welded 304L stainless steel. *Mater Des* 55:905–911. <https://doi.org/10.1016/j.matdes.2013.10.064>
21. Mondal AK, Biswas P, Bag S (2017) Experimental and FE analysis of submerged arc weld induced residual stress and angular deformation of single and double sided fillet welded joint. *Int J Steel Struct* 17:9–18. <https://doi.org/10.1007/s13296-016-0093-9>
22. Murugan N, Gunaraj V (2005) Prediction and control of weld bead geometry and shape relationships in submerged arc welding of pipes. *J Mater Process Technol* 168:478–487. <https://doi.org/10.1016/j.jmatprotec.2005.03.001>
23. Pandey C, Giri A, Mahapatra MM (2016) On the prediction of effect of direction of welding on bead geometry and residual deformation of double-sided fillet welds. *Int J Steel Struct* 16:333–345. <https://doi.org/10.1007/s13296-016-6007-z>
24. Parmar RS (2001) *Welding processes and technology*, 2nd edn. Khanna Publishers, Delhi
25. Piatti G, Vedani M (1990) Relation between tensile properties and microstructure in type 316 stainless steel SA weld metal. *J Mater Sci* 25:4285–4297. <https://doi.org/10.1007/BF00581086>
26. Piatti G, Vedani M (1989) Material variability in composition and structure of a Type 316 stainless steel submerged arc weld metal. *J Mater Sci* 24:1429–1438. <https://doi.org/10.1007/BF02397083>
27. Prasad K, Dwivedi DK (2008) Some investigations on microstructure and mechanical properties of submerged arc welded HSLA steel joints. *Int J Adv Manuf Technol* 36:475–483. <https://doi.org/10.1007/s00170-006-0855-1>
28. Shen S, Oguocha INA, Yannacopoulos S (2012) Effect of heat input on weld bead geometry of submerged arc welded ASTM A709 Grade 50 steel joints. *J Mater Process Technol* 212:286–294. <https://doi.org/10.1016/j.jmatprotec.2011.09.013>
29. Smith JJ, Farrar RA (2014) Influence of microstructure and composition on mechanical properties of some AISI 300 series weld metals. *Int Mater Rev* 38:25–51. <https://doi.org/10.1179/imr.1993.38.1.25>
30. Toma RE, Brandi SD, Souza AC, Moris Z (2011) Comparison between DC (+) and square wave AC SAW current outputs to weld AISI 304 for low-temperature applications. *Weld J* 90:153s–160s

31. Yadaiah N (2015) Experimental investigation and numerical modelling of deep penetration laser and GTA welding processes. IIT, Guwahati
32. Yang LJ, Chandel RS, Bibby MJ (1992) The effects of process variables on the bead width of submerged-arc weld deposits. *J Mater Process Technol* 29:133–144. [https://doi.org/10.1016/0924-0136\(92\)90430-Z](https://doi.org/10.1016/0924-0136(92)90430-Z)

**Publisher's Note** Springer Nature remains neutral with regard to jurisdictional claims in published maps and institutional affiliations.